



Cite this: DOI: 10.1039/d3mh01160g

Received 23rd July 2023,  
Accepted 14th September 2023

DOI: 10.1039/d3mh01160g

rsc.li/materials-horizons

# Micrometer-scale single crystalline particles of niobium titanium oxide enabling an Ah-level pouch cell with superior fast-charging capability†

Renming Zhan,<sup>id</sup> Shiyu Liu, Wenyu Wang, Ziheng Chen, Shuibin Tu,  
Xiancheng Wang, Hanlong Ge, Hongyu Luo, Tianqi Chai, Yangtao Ou, Yuchen Tan  
and Yongming Sun<sup>id</sup>\*

Wadsley–Roth phase niobium titanium oxide ( $\text{TiNb}_2\text{O}_7$ ) is widely regarded as a promising anode candidate for fast-charging lithium-ion batteries due to its safe working potential and doubled capacity in comparison to the commercial fast-charging anode material (lithium titanium oxide,  $\text{Li}_4\text{Ti}_5\text{O}_{12}$ ). Although good fast charge/discharge performance was shown for nanostructured  $\text{TiNb}_2\text{O}_7$ , the small size would cause the low electrode compaction density and energy density of batteries, as well as parasitic reactions. Fundamental understanding of the electrochemical lithium insertion/extraction process and the structural evolution for the micrometer-scale single crystalline  $\text{TiNb}_2\text{O}_7$  (MSC- $\text{TiNb}_2\text{O}_7$ ) could provide insights to understand its inherent properties and possibility for fast-charging application. Here, we revealed the highly reversible structural evolution of the MSC- $\text{TiNb}_2\text{O}_7$  during the lithiation/delithiation processes. Interestingly, an ion-conductive lithium niobate interphase was *in situ* formed on the MSC- $\text{TiNb}_2\text{O}_7$  surface during the formation cycle, which could facilitate fast ion diffusion on the material surface and support fast electrochemical reaction kinetics. Experimentally, the MSC- $\text{TiNb}_2\text{O}_7$  delivered a high reversible capacity of  $291.9 \text{ mA h g}^{-1}$  at 0.5C with a high initial Coulombic efficiency (>95%), and showed superb rate capability with a reasonable capacity of  $55.6 \text{ mA h g}^{-1}$  under a high current density of 40C. An Ah-level pouch cell with a lithium cobalt oxide ( $\text{LiCoO}_2$ ) cathode exhibited 91.5% capacity retention at 3C charging rate, which revealed the significant role of high crystallinity and *in situ* formation of an ion conductive nano-interphase in realizing fast charging capability of practical  $\text{TiNb}_2\text{O}_7$ -based lithium-ion batteries.

## Introduction

There is increasing demand for achieving superior fast charging capability of lithium-ion batteries to meet the various

Wuhan National Laboratory for Optoelectronics, Huazhong University of Science and Technology, Wuhan 430074, China. E-mail: yongmingsun@hust.edu.cn

† Electronic supplementary information (ESI) available. See DOI: <https://doi.org/10.1039/d3mh01160g>

### New concepts

Wadsley–Roth phase  $\text{TiNb}_2\text{O}_7$  has been extensively studied as a promising lithium-ion battery anode material due to its safe working potential and rationally high capacity. While much attention has been given to developing nanostructured  $\text{TiNb}_2\text{O}_7$  materials to pursue fast charging capability, their small size would lead to low electrode compaction density and energy density of batteries, as well as parasitic reactions between the electrolyte and active materials. In this work, fundamental investigation of the electrochemical lithium insertion/extraction processes and the structural evolution of micrometer-scale single crystalline  $\text{TiNb}_2\text{O}_7$  (MSC- $\text{TiNb}_2\text{O}_7$ ) were conducted, providing insights to understand its inherent properties. Superior fast-charging capability with 91.5% capacity retention for 3C charging rate was shown in an Ah-level  $\text{LiCoO}_2\|\text{MSC-TiNb}_2\text{O}_7$  pouch cell with a high anode compaction density of  $\sim 2.8 \text{ g cm}^{-3}$ .

applications in electric vehicles, portable electronics, and grid energy storage.<sup>1–7</sup> Graphite exhibits an intrinsic low potential of  $\sim 0.1 \text{ V}$  (close to 0 V, *vs.*  $\text{Li}^+/\text{Li}$ ). The large overpotentials involved during the rapid charging process may make the anode potential drop below 0 V (*vs.*  $\text{Li}^+/\text{Li}$ ) and prematurely terminate the electrochemical lithiation reactions, which, together with its sluggish lithium intercalation kinetics, leads to inferior fast-charging performance. Even worse, Li metal plating takes place at very low potentials, giving rise to major safety concerns.<sup>8,9</sup>  $\text{Li}_4\text{Ti}_5\text{O}_{12}$  is the most successful commercial fast-charging anode material, which possesses a safe operation potential ( $\sim 1.55 \text{ V}$  in average *vs.*  $\text{Li}^+/\text{Li}$ ) far above lithium plating and fast electrochemical lithium insertion/extraction reaction kinetics. Unfortunately, its unsatisfactory theoretical specific capacity ( $175 \text{ mA h g}^{-1}$ , only half of graphite), together with high working potential, significantly limits the energy density of batteries.<sup>10</sup> Wadsley–Roth phase  $\text{TiNb}_2\text{O}_7$  delivers a similar theoretical specific capacity and much safer working potential ( $387 \text{ mA h g}^{-1}$ ,  $\sim 1.65 \text{ V}$  in average *vs.*  $\text{Li}^+/\text{Li}$ ) in comparison to graphite ( $372 \text{ mA h g}^{-1}$ ,  $\sim 0.1 \text{ V}$  in average *vs.*  $\text{Li}^+/\text{Li}$ ), which could provide a large potential buffer for metallic

Li plating, making it a potential safe anode material for fast-charging lithium-ion batteries.<sup>11</sup> It is common knowledge that fast reaction kinetics requires high conductivity and fast Li<sup>+</sup> diffusion capability of the active materials, and inherent low ionic conductivity and sluggish Li<sup>+</sup> diffusion kinetics ( $\approx 10^{-15}$  cm<sup>2</sup> s<sup>-1</sup>) would lead to inferior fast-charging capability of the micrometer-scale bare TiNb<sub>2</sub>O<sub>7</sub> material with long charge transport distance.<sup>12,13</sup>

Several effective approaches have been explored and lead the direction of facilitating charge transport and electrochemical reaction based on nanomaterial design, including elemental doping (e.g., Cu<sup>2+</sup>, Mo<sup>6+</sup>, V<sup>5+</sup> and Zr<sup>4+</sup>),<sup>14–17</sup> composite structure construction (e.g., secondary nano-assembly and porous microsphere)<sup>18–21</sup> and surface engineering (e.g., carbon and Mexene coating).<sup>22–24</sup> Despite the exciting progress in achieving fast charge/discharge properties at the material level, nanostructures of the as-fabricated TiNb<sub>2</sub>O<sub>7</sub> would cause low compaction density of the electrode and serious parasitic reactions with the electrolyte due to the high accessible surface area.<sup>25,26</sup> Practical fast charging should be achieved at high mass loading and compaction density of the electrode with respect to the consideration of high energy density demand of batteries, which causes the contradiction between particle size and reaction kinetics in common knowledge. To date, fundamental understanding of the electrochemical reaction and structural stability of the MSC-TiNb<sub>2</sub>O<sub>7</sub> and investigation of the possibility for fast-charging applications are lacking.

Herein, an electrochemical reaction with high reversibility was revealed for MSC-TiNb<sub>2</sub>O<sub>7</sub> by *in situ* X-ray diffraction (XRD) and galvanostatic charge/discharge measurement, which explained its good electrochemical stability and suppressed the side reactions with the electrolyte. An ion-conductive Li-Nb-O interphase layer was observed on the MSC-TiNb<sub>2</sub>O<sub>7</sub> surface during the formation cycle, which, together with high crystallinity with low defect, enabled fast electrochemical reaction kinetics. As a result, the MSC-TiNb<sub>2</sub>O<sub>7</sub> delivered a high reversible specific capacity of 311.2 mA h g<sup>-1</sup> at 0.2C with a superior high initial Coulombic efficiency of 95%. Also, it displayed satisfying rate capability with a reasonably high capacity of 55.6 mA h g<sup>-1</sup> at 40C. To demonstrate the success of the MSC-TiNb<sub>2</sub>O<sub>7</sub> for fast charging lithium-ion batteries, an Ah-level pouch cell with a LiCoO<sub>2</sub> cathode achieved 91.5% capacity retention at 3C charging rate and good cycling stability, demonstrating the promise of the MSC-TiNb<sub>2</sub>O<sub>7</sub> for practical fast-charging lithium-ion batteries.

## Results and discussion

The lithium storage property of the MSC-TiNb<sub>2</sub>O<sub>7</sub> was evaluated by galvanostatic charge–discharge measurements at different C rates in both half and full cells. Satisfactorily, the MSC-TiNb<sub>2</sub>O<sub>7</sub> delivered an outstanding reversible specific capacity of 311.2 mA h g<sup>-1</sup> in the voltage range of 1–3 V at 0.2C with a high initial Coulombic efficiency of  $\sim$ 95% (Fig. S1, ESI<sup>†</sup>). Such a capacity was close to the theoretical value (312 mA h g<sup>-1</sup>) in

this specific voltage range, demonstrating a high material utilization ratio.<sup>12,27</sup> The high initial Coulombic efficiency indicated superior reversibility, which could be caused by the suppressed parasitic reactions between the active material and electrolyte due to the low surface area of the MSC-TiNb<sub>2</sub>O<sub>7</sub> (Fig. S2, ESI<sup>†</sup>).<sup>28</sup> We further investigated the rate performance of the MSC-TiNb<sub>2</sub>O<sub>7</sub>. Reversible specific capacities of 173 mA h g<sup>-1</sup> at 10C and small potential hysteresis of 0.4 V were displayed, which suggested good fast charge/discharge capacity of the MSC-TiNb<sub>2</sub>O<sub>7</sub> (Fig. 1a and b and Fig. S3, ESI<sup>†</sup>). It's worth noting that a reversible specific charge capacity of 55.6 mA h g<sup>-1</sup> could still be maintained at an extremely high current density of 40C. The MSC-TiNb<sub>2</sub>O<sub>7</sub> exhibits obvious superiority in rate performance in comparison to many reported TiNb<sub>2</sub>O<sub>7</sub>-based electrodes (Fig. S4, ESI<sup>†</sup>). The calculation of the pseudo-capacitance contribution for the MSC-TiNb<sub>2</sub>O<sub>7</sub> at different scanning rates suggested that the outstanding rate performance was mainly attributed to the fast Li<sup>+</sup> diffusion kinetics (Fig. S5, ESI<sup>†</sup>). Long-term cycling performance of the MSC-TiNb<sub>2</sub>O<sub>7</sub> was further carried out at 1C, and a high reversible specific charge capacity of 223 mA h g<sup>-1</sup> with a high capacity retention of 87.2% was achieved after 50 cycles (Fig. 1c and d). The average Coulomb efficiency reached 99.7% on cycling. A high reversible capacity of 135 mA h g<sup>-1</sup> at 0.5C and high capacity retention of 89% (calculated *via* capacity at 10C divided by the capacity at 0.5C) were achieved for the LiFePO<sub>4</sub>||MSC-TiNb<sub>2</sub>O<sub>7</sub> full cell (Fig. S6, ESI<sup>†</sup>), demonstrating the potential of the MSC-TiNb<sub>2</sub>O<sub>7</sub> for practical fast-charging lithium-ion batteries.

We then fabricated a practical Ah-level laminated LiCoO<sub>2</sub>||MSC-TiNb<sub>2</sub>O<sub>7</sub> pouch cell using a double-sided TiNb<sub>2</sub>O<sub>7</sub> anode with a high mass loading of  $\sim$ 17 mg cm<sup>-2</sup> and double-sided LiCoO<sub>2</sub> cathode with a high mass loading of  $\sim$ 24 mg cm<sup>-2</sup> (Fig. S7, ESI<sup>†</sup>). As a result, the LiCoO<sub>2</sub>||MSC-TiNb<sub>2</sub>O<sub>7</sub> pouch cell delivered a high initial charge/discharge capacity of 0.994 and 0.913 Ah during the formation process with a high initial coulombic efficiency of 90.4% (Fig. S8, ESI<sup>†</sup>). After the activation cycle, the pouch cell delivered a high reversible capacity of 0.906 Ah at 0.2C with an average discharge median voltage of 2.32 V. Surprisingly, with the current density increased from 0.2 to 0.5, 1, 2 and 3C, the pouch cell exhibited outstanding rate performance with reversible capacities of 0.885, 0.869, 0.85, and 0.829 Ah, respectively, and the corresponding capacity retention ratios were 97.7%, 95.9%, 93.8%, and 91.5%, respectively (Fig. 1e). It is worth emphasizing that the low voltage hysteresis for the LiCoO<sub>2</sub>||MSC-TiNb<sub>2</sub>O<sub>7</sub> pouch cell at different C rates could be maintained at 0.05, 0.06, 0.11, 0.18 and 0.26 V, which resulted in a high corresponding energy efficiency of 97.1%, 97%, 95.7%, 93.2%, and 90.6%, respectively (Fig. 1f and Fig. S9, ESI<sup>†</sup>). Besides, the LiCoO<sub>2</sub>||MSC-TiNb<sub>2</sub>O<sub>7</sub> pouch cell showed stable cycling under 1C, and an acceptable capacity of 0.738 Ah was maintained after 100 cycles with a rationally high capacity retention ratio of 82.9% (Fig. 1g and h).

Fig. 2a shows the XRD Rietveld refinement patterns of the MSC-TiNb<sub>2</sub>O<sub>7</sub>. The XRD peaks with high intensity verified the high crystallinity of the MSC-TiNb<sub>2</sub>O<sub>7</sub> without any impurities and the Rietveld refinement results revealed that the crystallization of the MSC-TiNb<sub>2</sub>O<sub>7</sub> followed a space group of

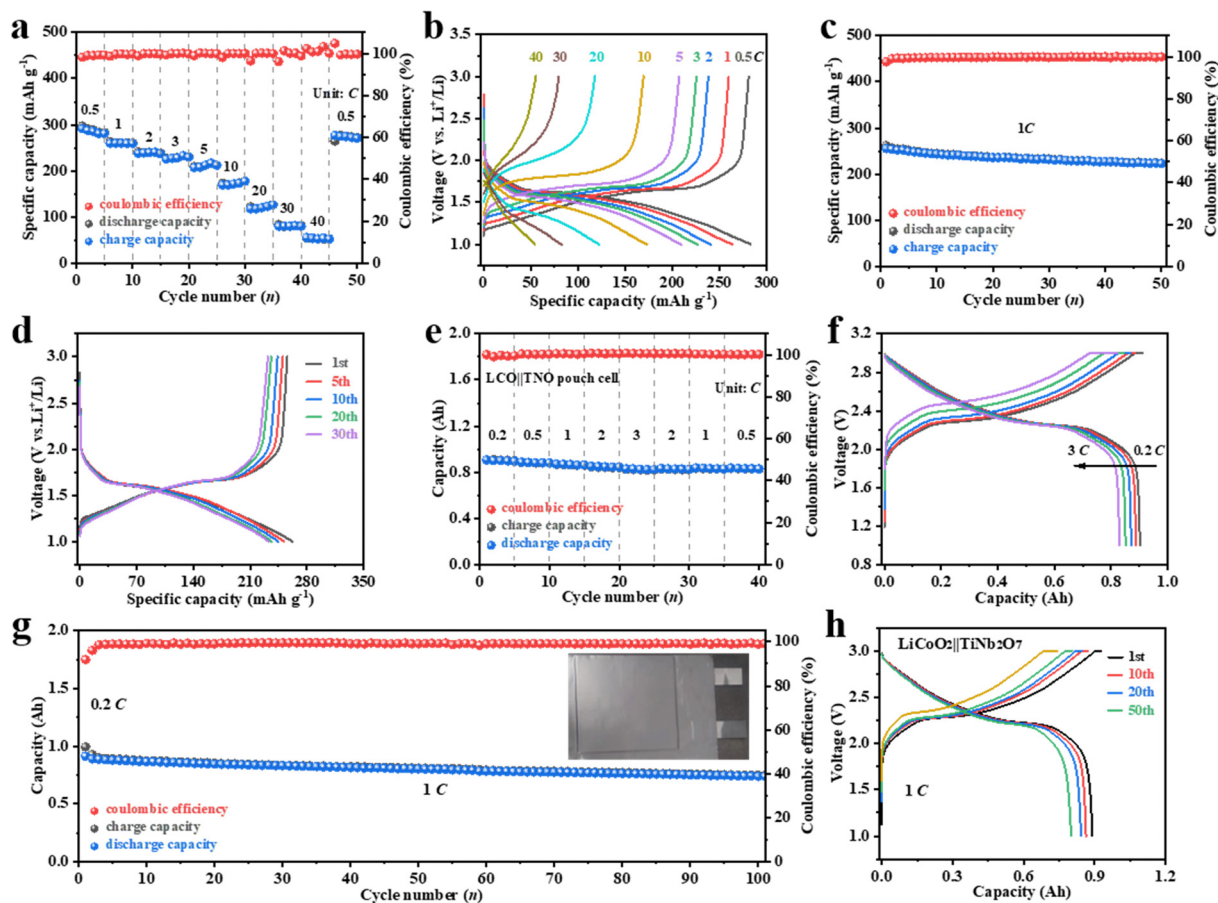


**Fig. 1** (a) The rate performance of the MSC-TiNb<sub>2</sub>O<sub>7</sub> and (b) the corresponding voltage-capacity plots at different C rates. (c) The cycling performance of the MSC-TiNb<sub>2</sub>O<sub>7</sub> at 1C (d) and the corresponding voltage-capacity plots for selected cycles. (e) The rate performance of the LiCoO<sub>2</sub>||MSC-TiNb<sub>2</sub>O<sub>7</sub> pouch cell and (f) the corresponding voltage-capacity plots for selected cycles. (g) The cycling performance of the LiCoO<sub>2</sub>||MSC-TiNb<sub>2</sub>O<sub>7</sub> pouch cell at 1C and (h) the corresponding voltage-capacity plots for selected cycles.

monoclinic  $C2/m$  and the lattice parameters were  $a = 20.37 \text{ \AA}$ ,  $b = 3.80 \text{ \AA}$ ,  $c = 11.89 \text{ \AA}$ ,  $\alpha = \gamma = 90^\circ$ , and  $\beta = 120.21^\circ$  (Tables S1 and S2, ESI<sup>†</sup>), which were in good agreement with previous publications.<sup>19,29</sup> The Rietveld refinement result further revealed uniform distribution of Nb and Ti ions at the 2a and 4i sites with a high cation distortion degree in the MSC-TiNb<sub>2</sub>O<sub>7</sub>, and the occupancy ratios of 66.7% Nb and 33.3% Ti for both sites, in accordance with the designed elemental ratio of 2/1 (Table S3, ESI<sup>†</sup>).<sup>30</sup> Nb element segregation was not detected in the MSC-TiNb<sub>2</sub>O<sub>7</sub> sample, which again supported its high crystallinity with few/ignorable defaults.<sup>31</sup> The well crystallized MSC-TiNb<sub>2</sub>O<sub>7</sub> with low default content explains the superior fast-charging capability and good structural stability during electrochemical cycling (Fig. 1).

The morphology and structure of the MSC-TiNb<sub>2</sub>O<sub>7</sub> sample were then investigated using a scanning electron microscope (SEM). The MSC-TiNb<sub>2</sub>O<sub>7</sub> displayed micrometer-scale single-particle features (1–3  $\mu\text{m}$ ), and a well-developed crystalline plane and straight edge, supporting its micrometer-scale single crystalline nature (Fig. 2b). High resolution transmission electron microscopy (HR-TEM) was used to further reveal the microstructure of the prepared MSC-TiNb<sub>2</sub>O<sub>7</sub> and uniform

structures were shown at a randomly selected area of a particle (Fig. 2c). To verify the single crystalline feature of the MSC-TiNb<sub>2</sub>O<sub>7</sub>, four regions on the particle in Fig. 2c were chosen for further evaluation, which were denoted as Region 1, Region 2, Region 3, and Region 4. Fig. 2(d)–(g) displays the corresponding fast-Fourier transform and inverse fast-Fourier transform results. With the zone axis of [124], the spots indexed to (40 $\bar{1}$ ) and (21 $\bar{1}$ ) were shown in all four regions (Tables S4 and S5, ESI<sup>†</sup>). Importantly, all these crystalline regions displayed the same crystal orientation. Such results confirm the continuous crystallization of the monoclinic TiNb<sub>2</sub>O<sub>7</sub> across the measured particle, again supporting the single crystalline feature of the as-fabricated MSC-TiNb<sub>2</sub>O<sub>7</sub>.

The structural evolution of the MSC-TiNb<sub>2</sub>O<sub>7</sub> during the initial charge/discharge processes was further monitored by *in situ* XRD measurement. Fig. 3a and b show the real time *in situ* XRD patterns and corresponding two-dimensional contour map of the MSC-TiNb<sub>2</sub>O<sub>7</sub> electrode at the voltage range from 1 to 3 V. Upon Li<sup>+</sup> intercalation, the unit cell parameters of the MSC-TiNb<sub>2</sub>O<sub>7</sub> increased, which led to cell volume expansion. During the initial discharging process (lithiation process), the characteristic (003) and (602) peaks of the MSC-TiNb<sub>2</sub>O<sub>7</sub>

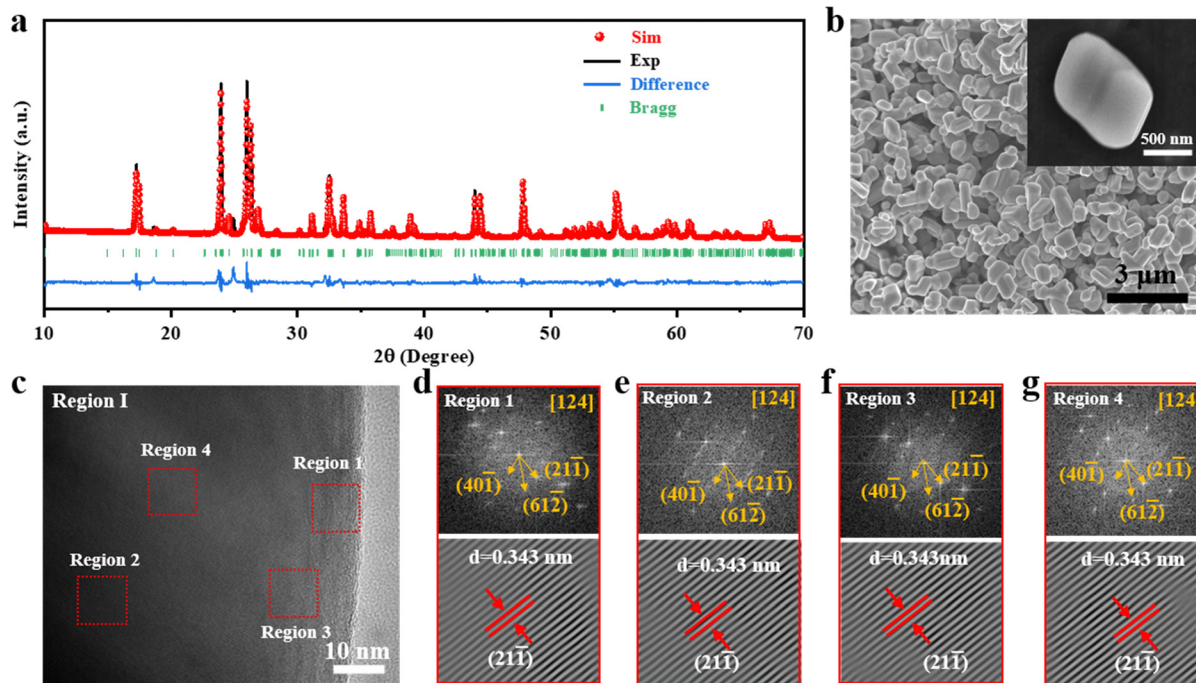


Fig. 2 (a) XRD patterns of the MSC-TiNb<sub>2</sub>O<sub>7</sub> with Rietveld refinement. (b) The SEM image of the MSC-TiNb<sub>2</sub>O<sub>7</sub>. (c) The sectional-region HR-TEM image of the MSC-TiNb<sub>2</sub>O<sub>7</sub>. (d)–(g) The fast-Fourier transform and corresponding inverse fast-Fourier transform of the selected region for the HR-TEM image.

shifted from the initial 26.0° and 26.3° before discharge to 25.93° and 26.31° after discharge (to 1 V) during the discharging process. In comparison to the large shift in previous publications, the slight shift of the (003) and (602) peaks verified the stable structure of the as-fabricated MSC-TiNb<sub>2</sub>O<sub>7</sub>.<sup>32</sup> Besides, the MSC-TiNb<sub>2</sub>O<sub>7</sub> displayed characteristic (110), (5 $\bar{1}$ 1) and (5 $\bar{1}$ 2) peaks at 24.0°, 32.5°, and 33.6° at open circuit voltage (OCV) and these peaks shifted to 22.02°, 30.83° and 32.49° after discharge to 1 V, respectively, which again supported its stable structure during the discharge process.<sup>14</sup> All the characteristic XRD peaks of the MSC-TiNb<sub>2</sub>O<sub>7</sub> came back to the original Bragg position at the full charge state with full Li<sup>+</sup> de-intercalation, suggesting that there was no irreversible phase transition and the MSC-TiNb<sub>2</sub>O<sub>7</sub> showed superior structural stability. Furthermore, characteristic peaks of (110), (5 $\bar{1}$ 1) and (5 $\bar{1}$ 2) were typically selected to investigate the detailed structural evolution of the MSC-TiNb<sub>2</sub>O<sub>7</sub> during the initial charge/discharge processes.

Three-dimensional (3D) surface maps shown in Fig. 3(c)–(e) revealed the asymmetric peak shift evolution for the charge and discharge processes, which could be attributed to different phase transition processes for Li<sup>+</sup> insertion and extraction and explain the asymmetric voltage plots.<sup>33–35</sup> The XRD peaks for (110), (5 $\bar{1}$ 1) and (5 $\bar{1}$ 2) were located at 24.0°, 32.5°, and 33.6° at the OCV before discharge, they were reduced to lower degrees after discharge to 1 V (vs. Li<sup>+</sup>/Li) and then went back to 23.9°, 32.5° and 33.6° after a full discharge/charge cycle. We further compared the lattice parameters of the MSC-TiNb<sub>2</sub>O<sub>7</sub> before and after a full charge/discharge cycle, and almost the same values of *a*, *b* and *c* were shown. Besides, no morphology and

structure change were observed for the cycled MSC-TiNb<sub>2</sub>O<sub>7</sub> at particle and electrode levels, suggesting the good structural integrity (Fig. 3(f)–(h) and Fig. S10, ESI†). Therefore, despite the asymmetric phase transition processes, complete structure recovery was achieved during the charge/discharge processes, which indicated the superior structural stability of the MSC-TiNb<sub>2</sub>O<sub>7</sub> and supported the satisfying electrochemical reversibility (Fig. 1).

X-ray photoelectron spectroscopy (XPS) measurement was used to further investigate the information of chemical states of the elements on the surface of the MSC-TiNb<sub>2</sub>O<sub>7</sub> during the initial charge/discharge processes. At the OCV state, the elemental signals of Nb and Ti were shown in the survey XPS spectrum (Fig. S11, ESI†). The high-resolution Nb 3d XPS spectrum showed two peaks 210.9 and 208.1 eV for Nb 3d<sub>3/2</sub> and Nb 3d<sub>5/2</sub>, respectively, which could be ascribed to Nb<sup>5+</sup> (Fig. 4a).<sup>36</sup> In the high-resolution Ti 2p XPS spectra, the two strong peaks at 465.5 and 459.6 eV could be assigned to Ti 2p<sub>1/2</sub> and Ti 2p<sub>3/2</sub> for Ti<sup>4+</sup>, respectively (Fig. 4b).<sup>33</sup> Besides, no Li signal was shown in the high-resolution Li 1s spectrum at the OCV state (Fig. 4c). Thus, the surficial chemical valence states of the elemental elements in the initial MSC-TiNb<sub>2</sub>O<sub>7</sub> were Ti<sup>4+</sup> and Nb<sup>5+</sup>.

In the high-resolution Nb 3d XPS spectrum, the characteristic peaks at 210.9 and 208.1 eV for Nb<sup>5+</sup> disappeared upon the lithiation process of the MSC-TiNb<sub>2</sub>O<sub>7</sub> electrode from OCV to 1.6 V (Li<sup>+</sup>/Li), and new peaks at 208.8 and 204.6, 206.5 and 203.6 eV were shown below 1.6 V (Li<sup>+</sup>/Li), which could be assigned to Nb<sup>4+</sup> and Nb<sup>3+</sup>, respectively.<sup>37</sup> When the electrode further discharged to 1.0 V, the dominating peaks for Nb<sup>3+</sup> were

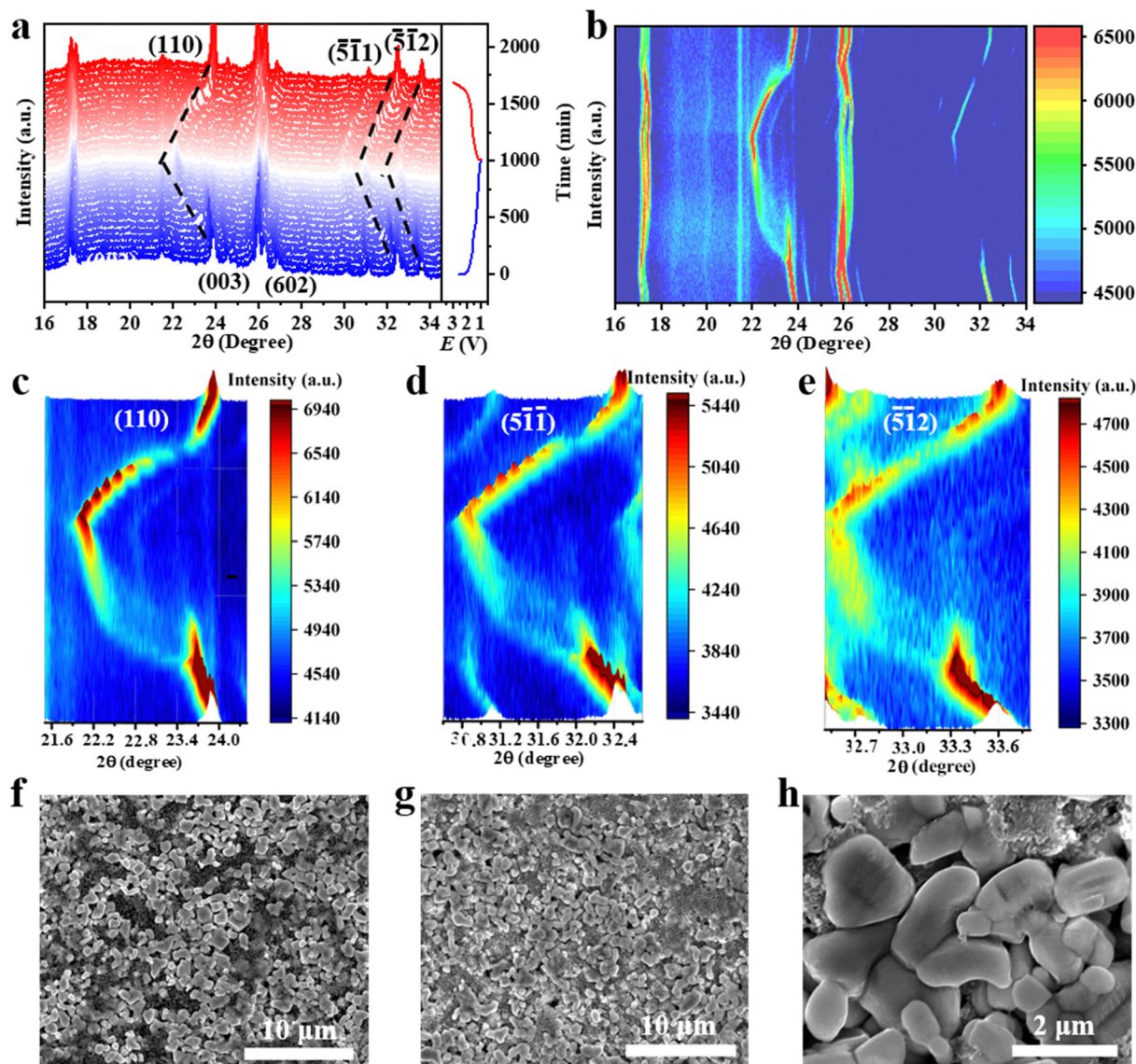


**Fig. 3** *In situ* XRD patterns of the MSC-TiNb<sub>2</sub>O<sub>7</sub> during the first discharge and charge processes in the voltage range between 1 and 3 V. (a) *In situ* XRD patterns and (b) the corresponding 2D contour map. (c)–(e) The 3D surface maps of (110) (c), ( $\bar{5}\bar{1}\bar{1}$ ) (d) and ( $\bar{5}\bar{1}\bar{2}$ ) peaks (e). (f) The SEM image of the fresh MSC-TiNb<sub>2</sub>O<sub>7</sub> electrode. (g) and (h) The SEM image of the MSC-TiNb<sub>2</sub>O<sub>7</sub> electrode after full charge/discharge processes.

shown. Interestingly, no characteristic peaks for Nb<sup>5+</sup> reappeared when the MSC-TiNb<sub>2</sub>O<sub>7</sub> electrode was again charged to 3.0 V, indicating the change of surficial chemical states after the formation cycle (Fig. 4a). In the high-resolution Ti 2p spectrum, characteristic Ti 2p peaks disappeared when discharged to 1.6 V, and they were not shown during the subsequent full charge/discharge processes (Fig. 4b). It's worth noting that the Li characteristic peak at 55 eV emerged in the high-resolution Li 1s XPS spectrum after being discharged to 1.6 V and it remained stable during the subsequent further discharge process and charge processes, which indicated the formation of lithium compounds/lithium-containing species on the electrode surface during the formation cycle.<sup>38</sup> To clearly reveal the evolution of surficial chemical states for different metal elements, 3D high-resolution Li 1s, Ti 2p, and Nb 3d XPS

spectra maps of the MSC-TiNb<sub>2</sub>O<sub>7</sub> electrode at different states of charge were demonstrated in Fig. 4d. It was concluded that the surface structure of the MSC-TiNb<sub>2</sub>O<sub>7</sub> changed and the initial Ti–Nb–O compound converted to a Li–Nb–O compound during the activation cycle. Since the ionic radii of Nb<sup>4+</sup> (0.68 Å) and Nb<sup>3+</sup> (0.72 Å) are close to Li<sup>+</sup> (0.76 Å), the Li/Nb exchange can take place during the discharge process, which supports the formation of Li–Nb–O species on the surface of the active material.<sup>39–41</sup> Importantly, the Li–Nb–O compound could often provide high Li<sup>+</sup> conductivity and enable fast electrochemical reaction kinetics, which explains the superior rate performance of the MSC-TiNb<sub>2</sub>O<sub>7</sub> (Fig. 1a).<sup>42,43</sup>

Dark-field TEM was employed to investigate the interfacial information of the MSC-TiNb<sub>2</sub>O<sub>7</sub> after the initial activation process. Fig. 5a and b show the HAADF-TEM image of an

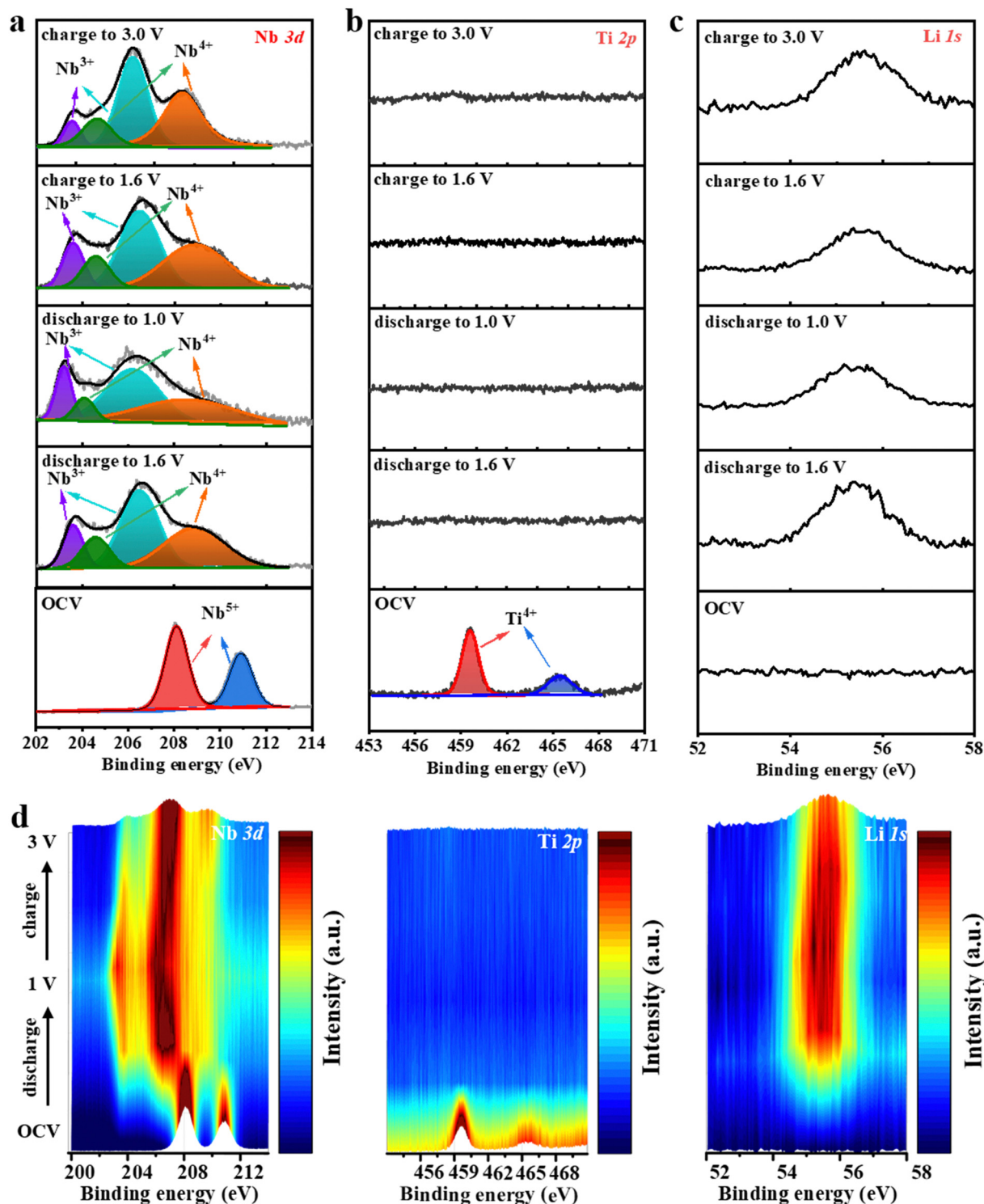


Fig. 4 (a)–(c) The high-resolution Nb 3d, Ti 2p, and Li 1s XPS spectra of the MSC-TiNb<sub>2</sub>O<sub>7</sub> electrode at different states of charge, and (d) the corresponding 3D high-resolution XPS spectra maps.

MSC-TiNb<sub>2</sub>O<sub>7</sub> particle and the corresponding EDS counts of Ti and Nb signals across the particle. EDS count-position plots in Fig. 5b revealed the stable intensity for Ti and Nb elements with a slight vibration in the inner of the bulk particle, revealing the constant Ti and Nb contents. In contrast to the coexistence of Ti

and Nb elements, only Nb element was shown on the very surface of the MSC-TiNb<sub>2</sub>O<sub>7</sub>, which suggested surface composition reconstruction after the activation cycle. The thickness for this Ti loss layer was recorded as 10–15 nm according to the EDS counts of Ti and Nb signals on the surface.

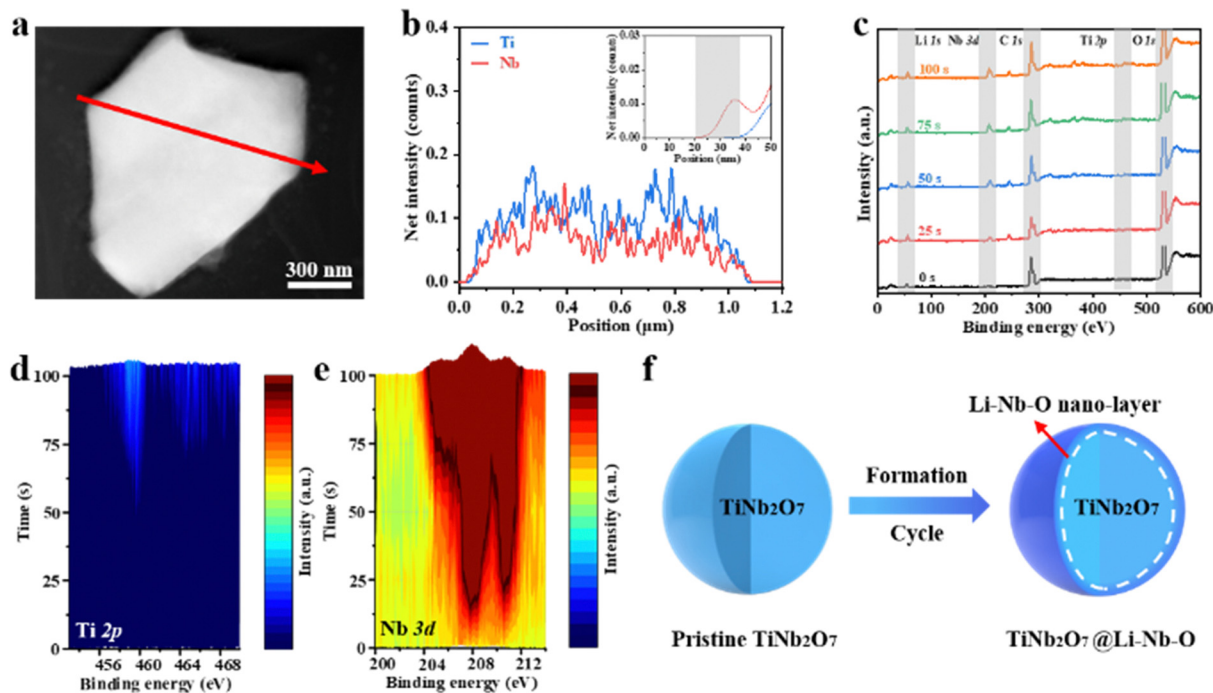


Fig. 5 (a) The dark-field TEM image of the MSC-TiNb<sub>2</sub>O<sub>7</sub> after the initial charge/discharge cycle. (b) EDS count-position plots across the MSC-TiNb<sub>2</sub>O<sub>7</sub> particle for Nb and Ti elements in (b) (red line). (c) Survey XPS spectra of the MSC-TiNb<sub>2</sub>O<sub>7</sub> with different sputtering times and the corresponding 3D high-resolution (d) Ti 2p and (e) Nb 3d XPS spectra. (f) Schematic illustration of the formation of an ion-conductive Li–Nb–O interphase layer on the MSC-TiNb<sub>2</sub>O<sub>7</sub> particle during the initial charge/discharge processes.

The surface component and structure reconstruction for the MSC-TiNb<sub>2</sub>O<sub>7</sub> was further studied by XPS depth measurement. Fig. 5c shows the survey XPS spectra of the MSC-TiNb<sub>2</sub>O<sub>7</sub> with different sputtering times, and Fig. 5d and e display the corresponding 3D high-resolution Ti 2p and Nb 3d XPS spectra, respectively. Besides the strong signal for O element, signals for Nb and Li elements were shown in the survey XPS spectra of the MSC-TiNb<sub>2</sub>O<sub>7</sub> at the initial state, and no Ti signal was observed at the initial state, which started to be shown after Ar<sup>+</sup> sputtering for 50s, supporting the formation of Li–Nb–O species on the electrode surface. The detailed information about the composition evolution on the electrode surface was recorded in the high-resolution Ti 2p XPS spectra and Nb 3d spectra. The intensity for the Ti signal gradually increased after its emersion at 50 s and reached a constant value at 75 s (Fig. 5d). Meanwhile, the high-resolution XPS spectra of the Nb 3d signal were augmented gradually with the increase of the sputtering time and stayed stable after 75 s (Fig. 5e). These results were consistent well with the *in situ* formation of the Ti loss surface layer by HAADF-TEM (Fig. 5b). The above measurement revealed that the initial electrochemical charge/discharge processes could induce the evolution of the surface composition and structure from the initial Nb–Ti–O to Li–Nb–O species, which may facilitate the reaction kinetics of the MSC-TiNb<sub>2</sub>O<sub>7</sub> (Fig. 5f).<sup>42,43</sup>

Li<sup>+</sup> diffusion behavior of the MSC-TiNb<sub>2</sub>O<sub>7</sub> was investigated by employing electrochemical impedance spectroscopy (EIS), the galvanostatic intermittent titration technique (GITT), and

cyclic voltammetry (CV). To study the evolution of the interphase property of the MSC-TiNb<sub>2</sub>O<sub>7</sub> during the formation cycle, EIS measurement was conducted before and after the initial cycle, and the resultant Nyquist plots are illustrated in Fig. 6a. The EIS plot of the fresh electrode was composed of two semicircles and one slope, and that after 1 cycle consists of one semicircle and one slope. The depressed semicircle denoted as R2 in the equivalent circuit at the high-frequency range could be ascribed to the electron transfer resistance for the fresh TiNb<sub>2</sub>O<sub>7</sub> electrode. The other depressed semicircle denoted as R3 at the medium-frequency region could be attributed to the Li<sup>+</sup> insertion resistance at the TiNb<sub>2</sub>O<sub>7</sub> particle surface. The slope could correspond to the Warburg resistance (W) in the low-frequency region, which reflects the charge state and reveals the Li<sup>+</sup> diffusion behavior at different charge states.<sup>44</sup> On the contrary, the MSC-TiNb<sub>2</sub>O<sub>7</sub> electrode after the formation cycle exhibited one semicircle and one slope, which could be ascribed to the electron transfer resistance and Li<sup>+</sup> diffusion behavior at the full charged state, respectively. Due to the formation of the Li–Nb–O compound on the MSC-TiNb<sub>2</sub>O<sub>7</sub> surface after the formation cycle, the value for R2 was reduced from 58.3 to 18.2 Ω after the formation cycle. More importantly, the Li<sup>+</sup> insertion resistance (R3) was significantly reduced from the initial 70.9 to close to 0 Ω after the initial charge/discharge cycle due to the formation of a thin Li–Nb–O nanolayer with high ionic conductivity. In addition, the reduced slope between the real impedance (Z') and reciprocal square root of angular frequency ( $\omega^{-1/2}$ ) at the low frequency for the cycled

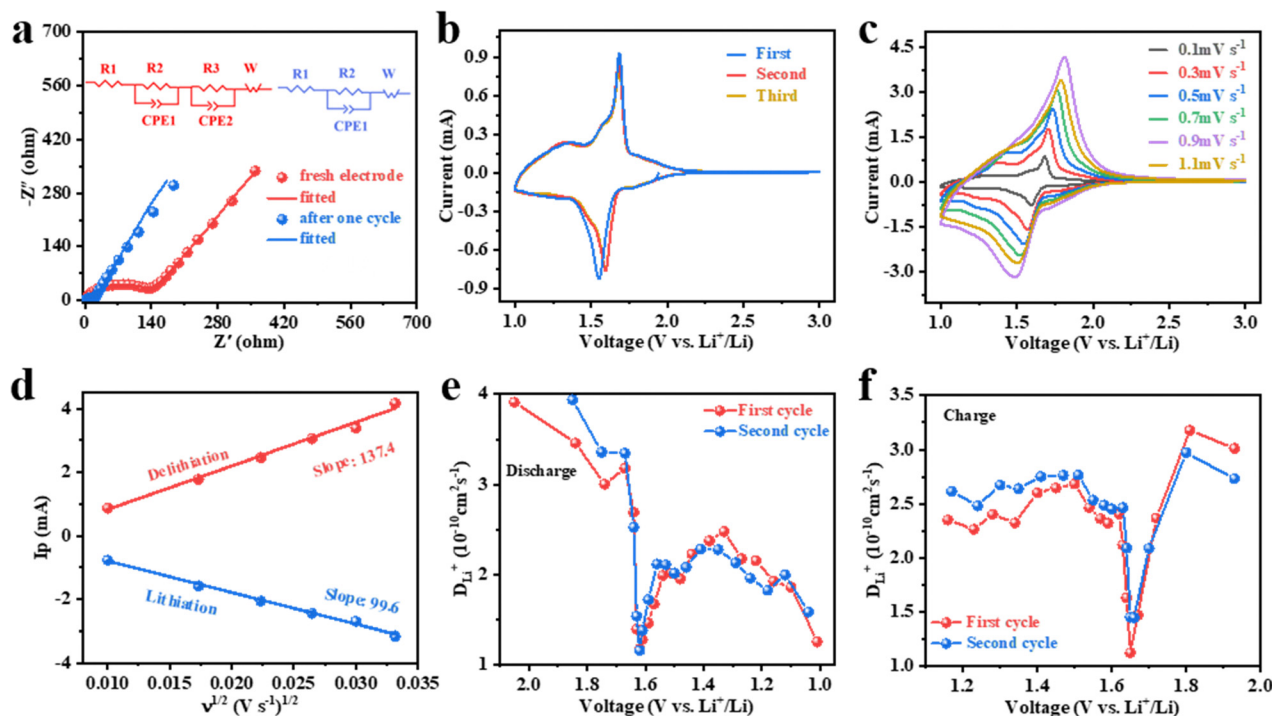


Fig. 6 (a) The Nyquist plots of the MSC-TiNb<sub>2</sub>O<sub>7</sub> electrode before and after the initial charge/discharge cycle, and the corresponding fitting results (inset shows the equivalent circuits). (b) The CV curves of the MSC-TiNb<sub>2</sub>O<sub>7</sub> electrode at 0.1 mV s<sup>-1</sup> for the initial three cycles. (c) CV curves of the MSC-TiNb<sub>2</sub>O<sub>7</sub> electrode at different sweep rates from 0.1 to 1.1 mV s<sup>-1</sup> and (d) the corresponding linear relationship plots between the square root of the scan rate ( $v^{1/2}$ ) and anodic/cathodic peak current ( $I_p$ ). The Li<sup>+</sup> diffusion coefficient of the MSC-TiNb<sub>2</sub>O<sub>7</sub> at the different (e) discharge and (f) charge states calculated by GITT profiles.

MSC-TiNb<sub>2</sub>O<sub>7</sub> suggested the enhanced Li<sup>+</sup> diffusion capability compared to the fresh MSC-TiNb<sub>2</sub>O<sub>7</sub> (Fig. S12, ESI†).

CV measurement was further used to reveal the electrochemical properties of the MSC-TiNb<sub>2</sub>O<sub>7</sub> at different scan rates from 0.1 to 1.1 mV s<sup>-1</sup> in the voltage range of 1–3 V. As shown in Fig. 6b and Fig. S13, ESI†, the initial three-cycle CV profiles were composed by three pairs of reversible redox couples corresponding to Nb<sup>3+</sup>/Nb<sup>4+</sup>, Nb<sup>4+</sup>/Nb<sup>5+</sup>, and Ti<sup>3+</sup>/Ti<sup>4+</sup>. The first-cycle CV curve showed a reduction peak at ~1.55 V, which shifted to ~1.60 V in the following two cycles. The reduced interphase resistance should be responsible for this change due to the formation of Li–Nb–O interphase on the MSC-TiNb<sub>2</sub>O<sub>7</sub> during the initial cycle. The good stability of such an interphase explained the well overlapped CV curves after the first cycle. This phenomenon verified the highly reversible electrochemical Li<sup>+</sup> insertion/extraction property of the MSC-TiNb<sub>2</sub>O<sub>7</sub> with a Li–Nb–O interphase. The CV curves at different scan rates were used to evaluate the lithium-ion diffusion capability (Fig. 6c). A linear relationship was shown between the square roots of the scan rates and the anodic/cathodic peak currents ( $I_p$ ) of the MSC-TiNb<sub>2</sub>O<sub>7</sub> electrode with the corresponding slopes of 137.4 and 99.6 for the anodic and cathodic scanning processes, respectively (Fig. 6d). The Li<sup>+</sup> diffusion coefficient ( $D_{Li}^+$ ) of the TiNb<sub>2</sub>O<sub>7</sub> electrode could be estimated by the slope obtained from the CV curves with different scanning rates according to the following equation:

$$I_p = 2.69 \times 10^5 An^{3/2} C_0 D^{1/2} v^{1/2}$$

Here,  $A$ ,  $n$ , and  $C_0$  were constants and marked as surface area, charge transfer number, and the molar concentration of Li<sup>+</sup> for the MSC-TiNb<sub>2</sub>O<sub>7</sub> electrode, respectively. Hence, the  $D_{Li}^+$  of the as-activated TiNb<sub>2</sub>O<sub>7</sub> electrode could be directly calculated by the ratio of scan rate ( $v$ ) and peak current ( $I_p$ ) at the anodic/cathodic process. In other words,  $D_{Li}^+$  increased with the value of the ratio. The high slopes suggested that the MSC-TiNb<sub>2</sub>O<sub>7</sub> electrode had fast Li<sup>+</sup> diffusion capability after the initial charge/discharge process. Furthermore, the discharge/charge GITT technique was further employed to verify the fast Li<sup>+</sup> diffusion capability of the MSC-TiNb<sub>2</sub>O<sub>7</sub>. As shown in Fig. S14, ESI† and Fig. 6e and f, the average Li<sup>+</sup> diffusion coefficients calculated by the GITT curves were  $2.17 \times 10^{-10}$  cm<sup>2</sup> s<sup>-1</sup> and  $2.43 \times 10^{-10}$  cm<sup>2</sup> s<sup>-1</sup> for the MSC-TiNb<sub>2</sub>O<sub>7</sub> at the first two cycles, respectively, which were better than those of TiNb<sub>2</sub>O<sub>7</sub> nanomaterials reported in the previous literature (Table S6, ESI†). The outstanding Li<sup>+</sup> diffusion capability explained the superior rate performance of the MSC-TiNb<sub>2</sub>O<sub>7</sub> (Fig. 1a).

## Conclusions

In summary, electrochemical lithium insertion/extraction reactions for MSC-TiNb<sub>2</sub>O<sub>7</sub> particles were investigated and highly reversibly structural evolution was revealed during the charge/discharge processes, which could support the stable material

structure for long-term cyclability. Also, it was revealed that an ionically conductive Li–Nb–O nano-interphase layer could be *in situ* electrochemically formed during the initial electrochemical activation process. The Li–Nb–O nano-interphase layer could effectively enhance the surficial lithium-ion transport capability, which, together with the high crystallinity of the bulk TiNb<sub>2</sub>O<sub>7</sub> single crystalline structure, could facilitate fast electrochemical reaction kinetics. Thus, the synergistic effects of the well crystalline TiNb<sub>2</sub>O<sub>7</sub> single crystal with low defects and ionically conductive Li–Nb–O nano-interphase layer could enable excellent electrochemical performance. As a result, the MSC-TiNb<sub>2</sub>O<sub>7</sub> electrode delivered a high specific charge capacity of 291.9 mA h g<sup>-1</sup> at 0.5C. Furthermore, we demonstrated that an Ah-level LiCoO<sub>2</sub>||MSC-TiNb<sub>2</sub>O<sub>7</sub> pouch cell delivered a high discharge capacity of 0.906 Ah at 0.2C and achieved a high capacity retention of 91.5% at 3C charging rate. This investigation revealed that surface reconstruction of certain micrometer-scale single-crystal intercalation-type electrode materials could promote fast electrochemical reaction kinetics and provides insights into using micrometer TiNb<sub>2</sub>O<sub>7</sub> particles for fast-charging lithium-ion batteries with reasonably high energy density.

## Author contributions

Y. S., R. Z., and S. L. conceived the idea and wrote the paper. W. W conducted the XRD Rietveld refinement. Z. C. performed the schematic drawing. S. T., H. G., C. T., and L. H. *et al.* contributed to the data recording and analysis.

## Conflicts of interest

The authors declare no conflict of interest.

## Acknowledgements

The authors acknowledge the Analytical and Testing Center of Huazhong University of Science and Technology for providing facilities for materials characterizations, including TEM, SEM and XRD.

## References

- 1 Y. Yang and J. Zhao, *Adv. Sci.*, 2021, **8**, 2004855.
- 2 K. Kang, Y. S. Meng, J. Breger, C. P. Grey and G. Ceder, *Science*, 2006, **311**, 977.
- 3 W. L. Cai, Y.-X. Yao, G.-L. Zhu, C. Yan, L.-L. Jiang, C. X. He, J.-Q. Huang and Q. Zhang, *Chem. Soc. Rev.*, 2020, **49**, 3806.
- 4 C.-Z. Ke, F. Liu, Z.-M. Zheng, H.-H. Zhang, M.-T. Cai, M. Li, Q.-Z. Yan, H.-X. Chen and Q.-B. Zhang, *Rare Met.*, 2021, **40**(6), 1347–1356.
- 5 C. Xu, L. Shen, W. Zhang, Y. Huang, Z. Sun, G. Zhao, Y. Lin, Q. Zhang, Z. Huang and J. Li, *Energy Storage Mater.*, 2023, **56**, 319–330.
- 6 L. Su, J. Ren, T. Lu, K. Chen, J. Ouyang, Y. Zhang, X. Zhu, L. Wang, H. Min, W. Luo, Z. Sun, Q. Zhang, Y. Wu, L. Sun, L. Mai and F. Xu, *Adv. Mater.*, 2023, **35**, 2205751.
- 7 C. Ke, R. Shao, Y. Zhang, Z. Sun, S. Qi, H. Zhang, M. Li, Z. Chen, Y. Wang, B. Sa, H. Lin, H. Liu, M.-S. Wang, S. Chen and Q. Zhang, *Adv. Funct. Mater.*, 2022, **32**, 2205635.
- 8 M. Baek, J. Kim, J. Jin and J. W. Choi, *Nat. Commun.*, 2021, **12**, 6807.
- 9 S. M. Lee, J. Kim, J. Moon, K. N. Jung, J. H. Kim, G. J. Park, J. H. Choi, D. Y. Rhee, J. S. Kim, J. W. Lee and M. S. Park, *Nat. Commun.*, 2021, **12**, 39.
- 10 S. Fu, X. Yu, Q. Wu, X. Yang, Z. Liu, X. Li, S. He, D. Wang, Y. Li, S. Tong and M. Wu, *Adv. Energy Mater.*, 2021, **11**, 2003270.
- 11 R. Zhan, D. Ren, S. Liu, Z. Chen, X. Liu, W. Wang, L. Fu, X. Wang, S. Tu, Y. Ou, H. Ge, A. J. Y. Wong, Z. W. Seh, L. Wang and Y. Sun, *Adv. Energy Mater.*, 2023, **13**, 2202544.
- 12 K. J. Griffith, I. D. Seymour, M. A. Hope, M. M. Butala, L. K. Lamontagne, M. B. Preefer, C. P. Koçer, G. Henkelman, A. J. Morris, M. J. Cliffe, S. E. Dutton and C. P. Grey, *J. Am. Chem. Soc.*, 2019, **141**(42), 16706–16725.
- 13 W. Xing, L.-E. Kalland, Z. Li, R. Haugsrud and J. Stevenson, *J. Am. Ceram. Soc.*, 2013, **96**, 3775–3781.
- 14 C. Yang, D. Ma, J. Yang, M. Manawan, T. Zhao, Y. Feng, J. Li, Z. Liu, Y.-W. Zhang, R. B. V. Dreele, B. H. Toby, C. P. de León Albarrán and J. H. Pan, *Adv. Funct. Mater.*, 2023, **33**, 2212854.
- 15 C. Lei, X. Qin, S. Huang, T. Wei and Y. Zhang, *ChemElectroChem*, 2021, **8**, 3379–3383.
- 16 K. Liu, J. Wang, J. Yang, D. Zhao, P. Chen, J. Man, X. Yu, Z. Wen and J. Sun, *Chem. Eng. J.*, 2021, **407**, 127190.
- 17 M. Yu, Z. Cai, Q. Li, S. Wang, Y. Ma, G. Song, W. Yang and C. Wen, *ACS Sustainable Chem. Eng.*, 2023, **11**, 5147–5154.
- 18 C. Jo, Y. Kim, J. Hwang, J. Shim, J. Chun and J. Lee, *Chem. Mater.*, 2014, **26**, 3508–3514.
- 19 B. Guo, X. Yu, X.-G. Sun, M. Chi, Z.-A. Qiao, J. Liu, Y.-S. Hu, X.-Q. Yang, J. B. Goodenough and S. Dai, *Energy Environ. Sci.*, 2014, **7**, 2220.
- 20 H. Park, H. B. Wu, T. Song, X. W. Lou and U. Paik, *Adv. Energy Mater.*, 2015, **5**, 1401945.
- 21 D. Pham-Cong, J. H. Choi, J. Yun, A. S. Bandarenka, J. Kim, P. V. Braun, S. Y. Jeong and C. R. Cho, *ACS Nano*, 2017, **11**, 1026–1033.
- 22 Y. Wu, D. Liu, D. Qu, J. Li, Z. Xie, X. Zhang, H. Chen and H. Tang, *Chem. Eng. J.*, 2022, **438**, 135328.
- 23 R. Qian, H. Lu, T. Yao, F. Xiao, J.-W. Shi, Y. Cheng and H. Wang, *ACS Sustainable Chem. Eng.*, 2022, **10**(1), 61–70.
- 24 T. Tian, L.-L. Lu, Y.-C. Yin, F. Li, T. Zhang, Y.-H. Song, Y.-H. Tan and H.-B. Yao, *Adv. Funct. Mater.*, 2021, **31**, 2007419.
- 25 Y. Sun, N. Liu and Y. Cui, *Nat. Energy*, 2016, **1**, 16071.
- 26 Z. Li, Z. Zhao, S. Pan, Y. Wang, S. Chi, X. Yi, J. Han, D. Kong, J. Xiao, W. Wei, S. Wu and Q.-H. Yang, *Adv. Energy Mater.*, 2023, 2300874.
- 27 X. Lu, Z. Jian, Z. Fang, L. Gu, Y.-S. Hu, W. Chen, Z. Wang and L. Chen, *Energy Environ. Sci.*, 2011, **4**, 2638.
- 28 Y. Wu, D. Liu, D. Qu, J. Li, Z. Xie, X. Zhang, H. Chen and H. Tang, *Chem. Eng. J.*, 2022, **438**, 135328.

- 29 J.-T. Han and J. B. Goodenough, *Chem. Mater.*, 2011, **23**, 3404–3407.
- 30 W. Wu, M. Liu, Y. Pei, W. Li, W. Lin, Q. Huang, M. Wang, H. Yang, L. Deng, L. Yao and Z. Zheng, *Adv. Energy Mater.*, 2022, **12**, 2201130.
- 31 N. V. Kosova, D. Z. Tsydpylyov, E. S. Papulovskiy and O. B. Lapina, *J. Phys. Chem. C*, 2022, **126**(32), 13607–13616.
- 32 X. Zhu, H. Cao, R. Li, Q. Fu, G. Liang, Y. Chen, L. Luo, C. Lin and X. S. Zhao, *J. Mater. Chem. A*, 2019, **7**, 25537.
- 33 Y. Yang, J. Huang, Z. Cao, Z. Lv, D. Wu, Z. Wen, W. Meng, J. Zeng, C. C. Li and J. Zhao, *Adv. Sci.*, 2022, **9**, 2104530.
- 34 K. Tang, X. K. Mu, P. A. van Aken, Y. Yu and J. Maier, *Adv. Energy Mater.*, 2013, **3**, 49.
- 35 B. Guo, X. Yu, X.-G. Sun, M. Chi, Z.-A. Qiao, J. Liu, Y.-S. Hu, X.-Q. Yang, J. B. Goodenough and S. Da, *Energy Environ. Sci.*, 2014, **7**, 2220.
- 36 H. Zhu, X. Cheng, H. Yu, W. Ye, N. Peng, R. Zheng, T. Liu, M. Shui and J. Shu, *Nano Energy*, 2018, **52**, 192–202.
- 37 T. Wang, T. Ge, S. Shi, M. Wu and G. Yang, *J. Alloys Compd.*, 2018, **740**, 7–15.
- 38 X. Yang, R. Liu, X. Xu, Z. Liu, M. Sun, W. Yan, D. Peng, C.-N. Xu, B. Huang and D. Tu, *Small*, 2021, **17**, 2103441.
- 39 V. Pralong, M. A. Reddy, V. Caignaert, S. Malo, O. I. Lebedev, U. V. Varadaraju and B. Raveau, *Chem. Mater.*, 2011, **23**, 1915–1922.
- 40 F. Xin, H. Zhou, Y. Zong, M. Zuba, Y. Chen, N. A. Chernova, J. Bai, B. Pei, A. Goel, J. Rana, F. Wang, K. An, L. F. J. Piper, G. Zhou and M. S. Whittingham, *ACS Energy Lett.*, 2021, **6**, 1377–1382.
- 41 X. Liu, T. Liu, R. Wang, Z. Cai, W. Wang, Y. Yuan, R. S. Yassar, X. Li, S. Wang, E. Hu, X.-Q. Yang, Y. Xiao, K. Amine, J. Lu and Y. Sun, *ACS Energy Lett.*, 2021, **6**, 320–328.
- 42 A. M. Glass, K. Nassau and T. J. Negran, *J. Appl. Phys.*, 1978, **49**, 4808–4811.
- 43 N. Özer and C. M. Lampert, *Sol. Energy Mater. Sol. Cells*, 1995, **39**, 367–375.
- 44 C. Yang, S. Yu, C. Lin, F. Lv, S. Wu, Y. Yang, W. Wang, Z.-Z. Zhu, J. Li, N. Wang and S. Guo, *ACS Nano*, 2017, **11**, 4217–4224.